Long-Pulse High-Performance Discharges in the DIII–D Tokamak

T.C. Luce,[1] M.R. Wade,[2] P.A. Politzer,[1] S.L. Allen,[3] M.E. Austin,[4] D.R. Baker,[1] B. Bray,[1] D.P. Brennen,[5] K.H. Burrell,[1] T.A. Casper,[3] M.S. Chu,[1] J.C. DeBoo,[1] E.J. Doyle,[6] J.R. Ferron,[1] A.M. Garofalo,[7] P. Gohil,[1] I.A. Gorelov,[8] C.M. Greenfield,[1] R.J. Groebner,[1] W.W. Heidbrink,[9] C.-L. Hsieh,[1] A.W. Hyatt,[1] R. Jayakumar,[3] J.E. Kinsey,[10] R.J. La Haye,[1] L.L. Lao,[1] C.J. Lasnier,[3] E.A. Lazarus,[2] A.W. Leonard,[1] Y.R. Lin-Liu,[1] J. Lohr,[1] M.A. Mahdavi,[1] M.A. Makowski,[3] M. Murakami,[2] C.C. Petty,[1] R.I. Pinsker,[1] R. Prater,[1] C.L. Rettig,[6] T.L. Rhodes,[6] B.W. Rice,[3] E.J. Strait,[1] T.S. Taylor,[1] D.M. Thomas,[1] A.D. Turnbull,[1] J.G. Watkins,[11] W.P. West,[1] and K.-L. Wong[8]

[1]General Atomics, P.O. Box 85608, San Diego, California 92186-5608, USA
email: luce@fusion.gat.com
[2]Oak Ridge National Laboratory, Oak Ridge, Tennessee 37831, USA
[3]Lawrence Livermore National Laboratory, Livermore, California 94550, USA
[4]University of Texas at Austin, Austin, Texas 78712, USA
[5]ORISE, Oak Ridge, Tennessee, USA
[6]University of California, Los Angeles, California 90095, USA
[7]Columbia University, New York, New York 10027, USA
[8]Princeton Plasma Physics Laboratory, Princeton, New Jersey 08543, USA
[9]University of California at Irvine, Irvine, California, USA
[10]Lehigh University, Bethlehem, Pennsylvania, USA
[11]Sandia National Laboratories, Albuquerque, New Mexico 87185-5800

Abstract. Significant progress in obtaining high performance discharges for many energy confinement times in the DIII–D tokamak has been realized since the previous IAEA meeting. In relation to previous discharges, normalized performance ~10 has been sustained for >5 τ_E with q_{min} >1.5. (The normalized performance is measured by the product $\beta_N H_{89}$ indicating the proximity to the conventional β limits and energy confinement quality, respectively.) These H–mode discharges have an ELMing edge and $\beta \lesssim 5\%$. The limit to increasing β is a resistive wall mode, rather than the tearing modes previously observed. Confinement remains good despite the increase in q. The global parameters were chosen to optimize the potential for fully non-inductive current sustainment at high performance, which is a key program goal for the DIII–D facility in the next two years. Measurement of the current density and loop voltage profiles indicate ~75% of the current in the present discharges is sustained non-inductively. The remaining ohmic current is localized near the half radius. The electron cyclotron heating system is being upgraded to replace this remaining current with ECCD. Density and β control, which are essential for operating advanced tokamak discharges, were demonstrated in ELMing H-mode discharges with $\beta_N H_{89} \sim 7$ for up to 6.3 s or ~34 τ_E. These discharges appear to be in resistive equilibrium with $q_{min} \sim 1.05$, in agreement with the current profile relaxation time of 1.8 s.

1. Introduction

The tokamak is the magnetic confinement concept which has achieved plasma parameters closest to those necessary for ignition — a plasma where energy transport losses are compensated by the energy deposited in the plasma by the fusion products. However, in conventional H–mode ignition scenarios [1], the required plasma current must be supplied inductively. This implies pulsed operation, which leads to engineering concerns about fatigue from mechanical and thermal cycling. Almost 30 years ago, it was recognized that finite particle orbits in the presence of plasma density and temperature gradients imply the existence of a self-generated or "bootstrap" current in a tokamak [2]. The existence of this bootstrap current opens the potential for steady-state in a tokamak. While the bootstrap current is a small fraction of the total current required in conventional H–mode scenarios, the theoretical possibility of current and pressure profiles consistent with both near-ignited operation, ideal MHD stability with an ideal conducting wall, and high bootstrap fractions has been shown [3].

High fusion gain scenarios which require no inductive current have been proposed based on modeling [3,4]. Since the current profile is no longer tied to the conductivity of the plasma,

the current and pressure profiles can be designed to maximize the ideal MHD stability and bootstrap current. The remaining current would be supplied by external non-inductive sources. The efficiency of these sources and the assumed energy transport set the upper limit on fusion gain in this modeling. Because this optimization can lead either to higher performance than conventional inductive scenarios or to a steady-state tokamak, these solutions are called “advanced tokamak” scenarios.

In a large tokamak, three very different time scales come into play — the Alfvén time (the time scale for ideal MHD instabilities to grow), the energy confinement time (the time scale for the pressure profile to equilibrate), and the current relaxation time (the time scale for the plasma current density profile to equilibrate). In DIII–D, the Alfvén time is <1 ms, the energy confinement time (τ_E) is 100–300 ms, and the current relaxation time (τ_R) is 1–3 s. The demonstration in the DIII–D tokamak of advanced tokamak plasmas for many energy confinement times is the subject of this paper.

In order to assess progress in advanced tokamak research, appropriate figures of merit must be defined. Initial advanced tokamak experiments demonstrated for times shorter than τ_E the existence of regimes with pressures and confinement well in excess of conventional scenario expectations [5]. The ideal stability limit of conventional scenarios is expected to be at $\beta_N \lesssim 3.5$ [$\beta_N \equiv \beta/(I/aB)$ in % m T/MA] while resistive modes are assumed to limit ignited plasmas to $\beta_N \leq 2.5$ [1]. (β is the ratio of the kinetic pressure to the magnetic pressure, I is the plasma current, a is the minor radius, and B is the toroidal magnetic field.) Confinement in standard ELMing H–mode can be described by specialized scaling relations derived from multi-machine databases [6]. The normalization used here will be the L–mode scaling relation known as ITER–89P developed as a part of the ITER design study [7]. Conventional ELMing H–mode scenarios in present-day tokamaks show $\tau_E/\tau_{ITER-89P} \equiv H_{89} \simeq 2$. Combining the stability and confinement expectations into a single figure of merit, the conventional H–mode scenario will have normalized performance ($\beta_N H_{89}$) ~ 5. Normalized performance >20 has been achieved transiently on DIII–D. The limits on the β_N achieved can be understood in terms of ideal MHD stability [8]. The next challenge is to demonstrate high normalized performance for many energy confinement times to show that the pressure profile has come to equilibrium. Clear progress has been made toward this goal as shown in Fig. 1. The significance of q_{min} for advanced tokamaks is that the bootstrap current is larger at fixed β for cases with larger q_{min}. The $\beta_N H_{89}$ ~ 7 shots are twice the previous duration, and normalized performance at fixed duration greater than 5 τ_E has been increased >25%. Most significantly for advanced tokamak research, the discharges with $\beta_N H_{89}$ ~ 9–10 have q_{min} > 1.5 which implies a larger bootstrap current fraction ($f_{BS} \equiv I_{BS}/I$). The long duration of this high normalized performance indicates that the evolution of the current profile, not the pressure profile is the cause of the loss of performance. Since

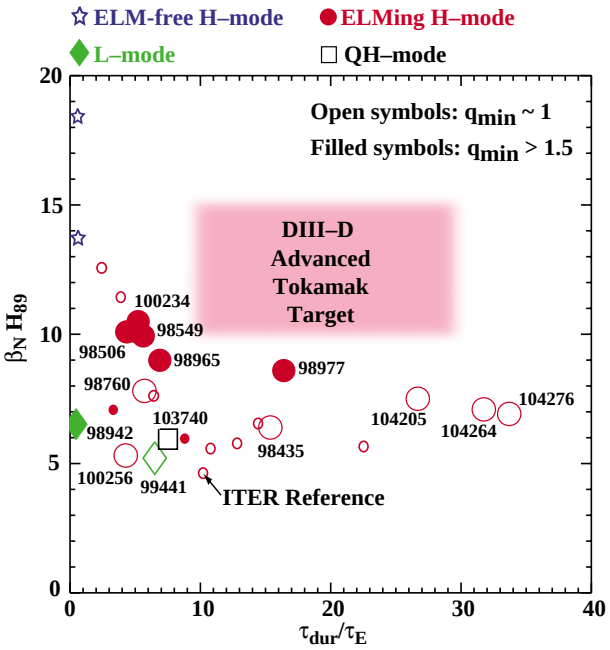

FIG. 1. Normalized performance vs. the ratio of the duration of the high performance phase to the energy confinement time. The larger symbols are discharges from the 1999 and 2000 DIII-D experimental campaigns. The smaller symbols are selected discharges from earlier campaigns [9]. The symbol type signifies the edge conditions in which the high performance was obtained: star is ELM-free H mode, circle is ELMing H mode, square is quiescent H mode, and diamond is L mode. An open symbol indicates q_{min} ~ 1, while a filled symbol indicates q_{min} > 1.5.

these discharges require considerable inductive current, the current profile diffuses toward resistive equilibrium. In principle, sustainment of the current profiles already achieved would yield high performance discharges limited only by engineering constraints of the tokamak system.

Another figure of merit for advanced tokamak scenarios is a comparison of the fusion gain and the bootstrap fraction with those achieved with a conventional inductive scenario. For a plasma of fixed shape and size at a given B, the fusion gain is thought to maximize at the maximum plasma current or minimum safety factor at the 95% poloidal flux surface (q_{95}). To minimize the probability of disruptions, the lowest practical q_{95} is normally taken to be >3 [1]. The 0-D fusion gain scales like $\beta\tau$. For high f_{BS}, higher q_{min} and q_{95} will be necessary. For fixed shape, size, and B, this requires lower I. If β_N and H_{89} are constant, fusion gain would drop proportional to I^2. The bootstrap current fraction, however, increases proportional to β_p, so at fixed β_N, $f_{BS} \propto I$. The key element of the advanced tokamak approach is that the current profiles are tailored such that the limiting β_N is much higher than in the conventional scenarios, thereby recovering part or all of the drop in fusion gain from the reduction in current while further increasing f_{BS}. The relative fusion gain also depends on the change in the energy confinement due to the optimized current profiles. This trade-off is illustrated in Fig. 2 for the sames discharges in shown in Fig. 1. Of special interest are the pair linked by the arrow in the figure, which have the same size, shape, and β. At the left end is a sawtoothing, ELMing H–mode discharge with q_{95} = 3.1. At the right is the discharge with $\beta_N H_{89}$ ~ 10 for ~5 τ_E at q_{95} = 5.5. The fusion gain indicator has dropped by 25% while the bootstrap fraction indicator has increased 230%. (Note that the actual fusion gain and f_{BS} depend on the details of the radial profiles.) The expected decrease in fusion gain at fixed $\beta_N H_{89}$ would be almost 70% and expected increase in f_{BS} only 180%. By breaking the correlation of the current profile with the conductivity, a significant improvement in the β limit has been gained with a coincident improvement in confinement.

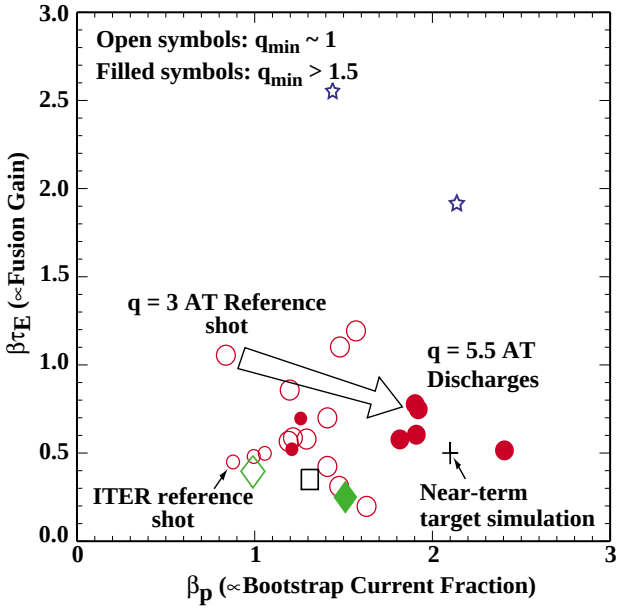

FIG. 2. $\beta\tau_E$ vs. β_p. The symbols are the same as shown in Fig. 1. The cross symbol shows the design point of a fully non-inductive advanced tokamak scenario consistent with the near-term hardware capabilities of DIII-D.

The time histories of several key parameters are shown in Fig. 3 for the $\beta_N H_{89}$ ~ 10 discharge. The neutral beam power is turned on early in the current ramp [Fig. 3(a)] to raise the conductivity and delay the penetration of the inductive current to the core [10]. This leaves the central safety factor q(0) high. The heating rate and current ramp rate are designed to give only a slightly reversed q profile at the end of the current ramp as shown in Fig. 3(b). The plasma is biased upward to keep the plasma in L mode. (In this configuration, the ∇B drift is away from the active divertor null.) Shortly after the end of the current ramp, the plasma configuration is made up-down symmetric. This shape change has several beneficial effects. The equalization of nulls is essentially an elongation ramp-up which leads to an increase in the internal inductance, ℓ_i. This increase is favorable for stability. The shape change also lowers the L–H transition threshold, leading to a transition within 100 ms. This is important to avoid internal MHD modes driven by the steep pressure gradients in the core [8]. The L–H transition also raises the electron temperature significantly, further slowing the current profile evolution. It is essential that the transition occur after the current ramp to avoid driving current inductively in the edge, which would lower ℓ_i. Optimization of the heating profile, current ramp rate, and

L–H transition timing has been carried out empirically. The time history of β_N is compared to 4 ℓ_i in Fig. 3(c). As a general guideline, the ideal MHD limit in the absence of a conducting wall is approximately 4 ℓ_i [11]. The stability of this discharge will be more extensively discussed in the next section. The discharge transitions from ELM-free H mode to ELMing H mode [Fig. 3(a)] without the global instability which terminated VH–mode plasmas [12]. The normalized performance $\beta_N H_{89}$ ~ 10 for >800 ms or ~5 τ_E. During the high performance phase, slowly growing n=1 magnetic perturbations are observed on saddle coils outside the vacuum vessel [Fig. 3(e)]. The current profile continues to evolve during this phase as can be seen by the continuous drop in q_{min} [Fig. 3(b)] and ℓ_i [Fig. 3(c)]. Eventually, an m=2/n=1 tearing mode is triggered [Fig. 3(e)] and the high performance phase in this discharge is irreversibly lost.

The discharge shown in Fig. 3 will serve as an example of a class of discharges which are being investigated for fully non-inductive high-performance operation in the DIII–D tokamak. In the following sections, the stability, energy transport, and current profile evolution of this type of discharge will be discussed in detail. The paper will conclude with demonstration in ELMing H mode of some of the control tools necessary to realize such an advanced tokamak discharge.

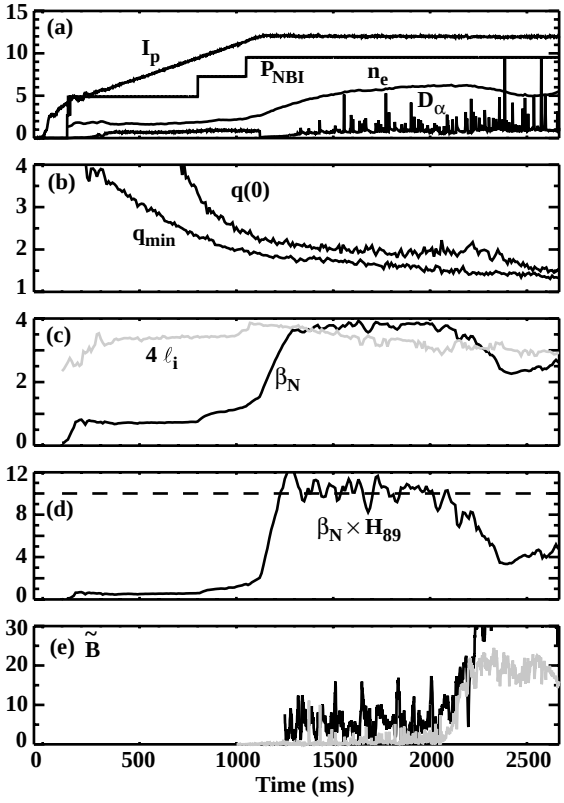

FIG. 3. Plasma parameters vs. time for a discharge (98549) with $\beta_N H_{89}$ ~ 10 for 5 τ_E. (a) From top to bottom: 10x plasma current (MA), neutral beam injected power (MW), line-averaged density (10^{19} m^{-3}), divertor D_α (a.u.); (b) q(0) (upper trace), q_{min} (lower trace); (c) β_N (darker trace), 4 x ℓ_i (lighter trace); (d) $\beta_N H_{89}$, dashed line $\beta_N H_{89}$ = 10; (e) n=1 saddle loop signal x10 (G) (darker trace), n=1 Mirnov amplitude (G) (lighter trace). The toroidal field is constant at 1.6 T. During the high performance phase, τ_E ~ 160 ms.

2. Stability

The key modes for describing the stability of discharges like that shown in Fig. 3 are the resistive wall mode, the tearing mode, and the Alfvèn mode destabilized by fast ions.

A. Resistive wall modes

Experimental and theoretical studies have shown that, under a variety of conditions in DIII-D, the ideal MHD limit in the absence of a conducting wall is due to an n=1 kink mode destabilized when $\beta_N \leq 4\ \ell_i$ [11]. With a perfectly conducting wall, the ideal mode β limit should be substantially higher. However, in the presence of a resistive wall, a mode similar in perpendicular displacement to the ideal mode is predicted [13]. The characteristics of this resistive wall mode (RWM) are a real frequency and growth rate on the time scale of the resistive time scale of the wall (~5 ms for DIII–D). This mode should appear when the β exceeds the no-wall ideal β limit. In Fig. 3(c), there are frequent drops in the β_N trace despite steady heating. These are correlated with nearly stationary n=1 magnetic perturbations detected outside the vacuum vessel by saddle loops. A particularly clear example of this mode is shown in Fig. 4. The detected perturbation is clearly n=1. The saddle loop measurements show a mode with a real frequency in the laboratory frame of ~100 Hz and growth on a time scale of ~10 ms, as predicted for the RWM. Ideal MHD analysis of the n=1 mode of the equilibrium reconstruction at 1900 ms of the discharge shown in Fig. 3 using the GATO code

[14] shows that the plasma is unstable without a wall and stable with a wall, again as predicted for the RWM. The appearance of slowly growing and rotating n=1 modes on the saddle coils when $\beta_N > 4\ \ell_i$ in a large number of similar shots [15], coupled with stability calculations and analysis in a smaller number of cases, leads to the conclusion that the resistive wall mode is the instability which limits the magnitude of β in this class of discharges.

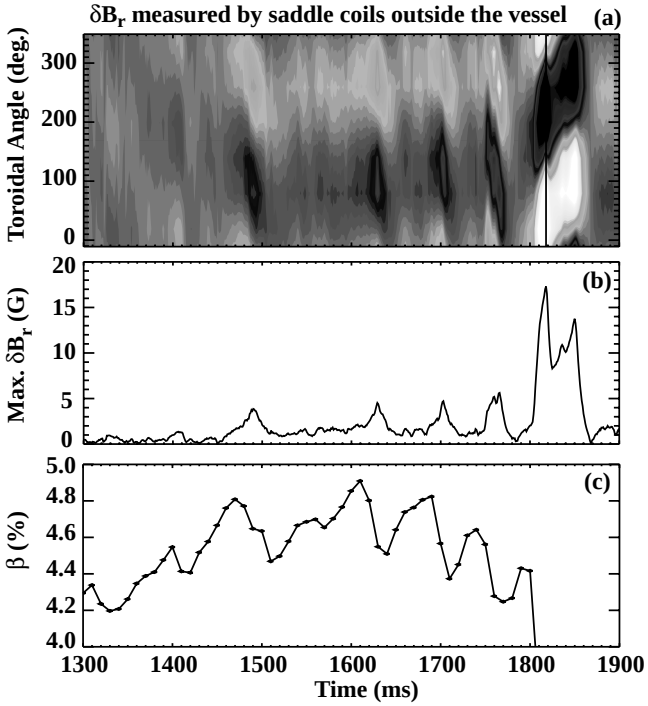

FIG. 4. (a) Contour plot of radial magnetic field measured by saddle loops outside the vacuum vessel vs. toroidal location and time. White and black areas are perturbations of opposite polarity; (b) maximum radial field (G) from the saddle loops vs. time; (c) β (%) vs. time. Note suppressed zero on vertical axis.

One surprising feature of these resistive wall modes (RWMs) is that they do not always grow to the disruptive limit or saturate. It appears that smaller RWMs cause a rapid dissipation of the edge pressure and current profiles which drive the mode. (Note that RWMs at the limit of detection (~1 G) have an observable effect on the plasma.) The changes in edge pressure, current, and divertor D_α suggest a reconnection near the edge, but it has not been determined experimentally whether the reconnection is due to the n=1 mode or some higher n mode is destabilized by it. The large RWMs such as the one at 1800 ms in Fig. 4 cause a substantial reconnection across the plasma. During the instability at 1800 ms, the plasma stored energy drops by 85%, the plasma current drops by almost 10% and the central current density increases by 50% within 30 ms. This lends some weight to the direct reconnection of the n=1 mode as the cause of the current and energy dissipation in the case of the smaller RWMs. A complete stability picture must include the effect of rotation on the instability and vice versa. Models which couple rotation and mode amplitude [16] can explain qualitatively the appearance of small and large RWMs and a two time-scale growth rate like that at 1800 ms in Fig. 4, but underestimate the critical rotation frequency by an order of magnitude [15].

B. Tearing modes

Previous reports on long-pulse high performance identified neoclassical tearing modes (NTMs) as the limit to increasing β in discharges with an ELMing H mode edge [9]. As discussed above, the limitation to increasing β in discharges such as the one shown in Figs. 3 and 4 is the resistive wall mode. The present discharges have $q_{min} > 1.5$ until the end of the high performance which excludes the possibility of an m=3/n=2 tearing mode. They are similar to the higher q_{min} discharges discussed in Ref. [9], but are achieved by different means. The present discharges are found to be significantly more stable to NTMs for about $0.5\ \tau_R$. This suggests the current profile is the key element for stability.

An attempt to map out the stability boundaries of the 2/1 tearing mode for the discharge in Fig. 3 is given in Fig. 5. The solid curve is the time independent solution of the Rutherford equation modified to include the perturbation of the bootstrap current by the island. At low β_p, all perturbations decay to 0. At some minimum value of β_p (here $\beta_p \sim 0.7$), perturbations larger than a threshold size (shown by the near vertical left side of the curve) will grow until they reach saturation (right side of the curve). The shape of the curve shown is determined from experimental measurements at 1900 ms. Superimposed is a time history of the measured β_p and an estimate of the island width from external magnetic measurements. Because of the

difficulty in evaluating Δ' precisely, an estimate is obtained by shifting the curve to match the measured β_p with the saturated width. (The effect of varying Δ' is a rigid shift of the curve in the vertical direction. More negative Δ' shifts the curve upward as expected for increased stability.) Further details of the determination of the stability curve and the experimental trajectory can be found in Ref. [17].

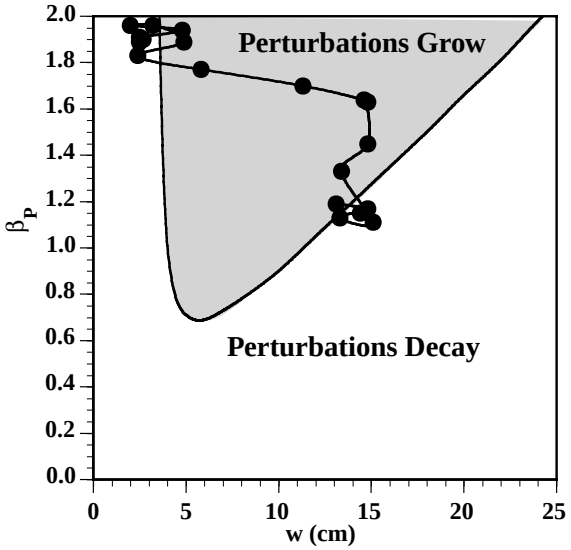

FIG. 5. Diagram of neoclassical tearing mode behavior according to the modified Rutherford equation. The solid line is the solution to the equation for stationary modes (dw/dt = 0) for the discharge in Fig. 3 at 1900 ms. The points connected by lines are the time history of the same discharge from 1700-2600 ms in β_p - w space at 50 ms intervals. The vertical position of the stationary mode curve is normalized to the time history as discussed in the text.

The agreement of the experimental trajectory with the stability boundary is striking. However, this result does not indicate the cause of the NTM. If the stability curve were static in time, then the triggering of the mode would be a statistical process where a large seed will occur eventually. This is inconsistent with the experimental observations that the NTMs reproducibly appear after about 900 ms in the high performance phase. During this period, the stability curve likely varies significantly as a result of changes in the current and ion temperature profiles. It is conjectured that this dynamic variation of the stability curve is the reason for the delayed onset of the NTMs in this case. More work is required to clarify this point, but if true, maintaining the current and density profiles in their earlier state when the plasma was stable to NTMs is the key to avoidance of the NTMs.

C. Alfvén modes

The Alfvén modes play a smaller role in the stability picture than the RWM or the NTM. They arise due to the presence of the fast ions from the neutral beam heating. The fraction of the total stored energy which is fast ions early in the high performance phase is about 20%, dropping to about 15% as the density rises. After the L–H transition, the stored energy rises rapidly, as shown in Fig. 6 for a discharge similar to the one in Fig. 3. The stored energy plateaus before the end of the ELM-free period, coincident with the onset of bursts of high frequency magnetic oscillations (f ~ 100–150 kHz). A slight rise and modulation of the D_α signal indicates a direct influence of the modes on energy loss to the divertor. Spectral analysis of these modes indicates discrete spectral peaks corresponding to n = 4–7. The plasma frame frequency is found to be 55 kHz, consistent with Alfvén gap structure calculations of the gap opened by finite β effects. These modes have the beneficial effect of softening the impact of the first ELM, which terminated the high performance in VH–mode plasmas [12]. The real-time β control has demonstrated the ability to regulate the plasma stored energy in a similar fashion (discussed in Section 5). Therefore, absence of the Alfvén mode will not be detrimental to this advanced tokamak scenario.

3. Transport

A. Energy transport

As discussed in the introduction, the improvement in stability through changes in the current profile cannot come at the expense of significantly increased energy transport if high fusion gain is the goal. The matched pair of discharges at each end of the arrow in Fig. 2 provide a good basis for studying the influence of the current profile changes on transport. The plasma shape, size, and toroidal field are kept constant and only the plasma current is varied to

change q_{95} from 5.5 to 3.1. No attempt was made to alter the q profile in the low q_{95} case, so sawtooth oscillations begin in the current ramp and continue through the discharge. The effective (one-fluid) heat diffusivity (χ_{eff}) for both discharges is shown in Fig. 7(a). The density is too high in the low-q case to separate the electron and ion fluxes. The two discharges have similar χ_{eff} in the core, while the high-q discharge has significantly higher χ_{eff} in the outer 40% of the plasma. Both neoclassical transport and transport from ion temperature gradient (ITG) modes near marginal stability are expected to vary like q^2 [18]. Dimensionless scaling experiments which varied only q measured empirically a scaling consistent with q^2 [19]. Since the ion temperature T_i and the ratio of the ion to electron temperature T_i/T_e are about the same in the outer half of both plasmas, the main difference in the two discharges is the change in q and the change in the density scale length. The collisionality is also higher in the low-q case, but measurements of the collisionality scaling would predict a weak increase in χ_{eff} with collisionality [20]. The ratios of χ_{eff} and q for the two discharges are shown in Fig. 7(b). The difference in χ_{eff} does not appear strongly correlated with the change in q^2. The main conclusion from this comparison is that the energy confinement is not severely degraded at the higher q.

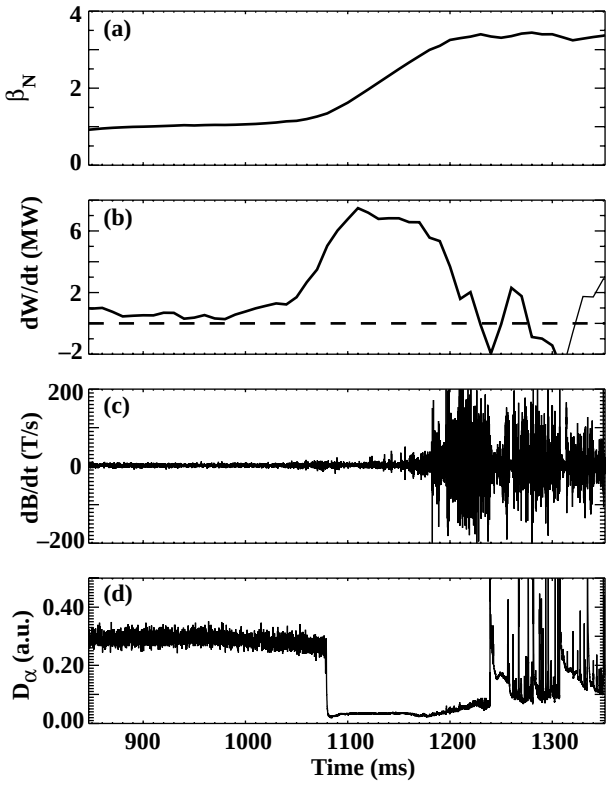

FIG. 6. Evidence for Alfvén mode activity limiting the β rise. (a) β_N vs. time; (b) dW/dt (MW) vs. time; (c) dB/dt (T/s) from internal magnetic probes vs. time; (d) divertor D_α (a.u.) vs. time.

The electron and ion diffusivities can be separated in the high q_{95} case. There is a significantly smaller ion diffusivity χ_i in the central region compared to the electron diffusivity. There is not a dramatic break in the measured ion temperature profile [Fig. 7(d).] at this point. The neoclassical ion diffusivity prediction is also shown in Fig. 7(c) for comparison. The measured χ_i is still higher than the neoclassical value.

The observation that χ_i is larger than neoclassical is consistent with simulations of the T_e and T_i profiles using χ_e and χ_i as determined by the GLF23 transport model, shown by the solid and dashed lines in Fig. 7(d) [21]. This model is a gyrofluid representation of the transport due to ITG modes, trapped electron modes, and ETG modes, including the effect of ExB shear on the mode spectrum. The experimental density and toroidal momentum are used as input, as are the model calculations of the heat sources. The electron-ion exchange term is self-consistently calculated as the T_e and T_i profiles change. The only adjustable parameter is the numerical coefficient multiplying the ExB shearing rate. A linear, no-threshold model is used for the effect of ExB shear. The agreement between the calculated and measured T_i profiles is excellent, and the agreement for the T_e profile is also very good. The model predicts that the turbulence is not completely suppressed, but is close to the marginal stability point — the growth rate is only slightly larger than the ExB shearing rate (Fig. 8).

This approach to a comparison between model and experiment, comparing predicted and measured profiles, is much more robust than the approach which uses smooth profiles fitted to the experimental data as input to the calculation of the maximum growth rate. For the

example shown in Fig. 8, the smooth profiles give a maximum growth rate smaller than the ExB shearing rate, and thus would indicate complete suppression of the turbulence. The difficulty with using the fitted profiles is the sensitivity of the growth rate to very small changes in the fit, particularly when near marginally. We should note that even the first approach used fitted profiles of density and toroidal momentum as inputs. The sensitivity of the modeling result to small variations in these inputs is not known.

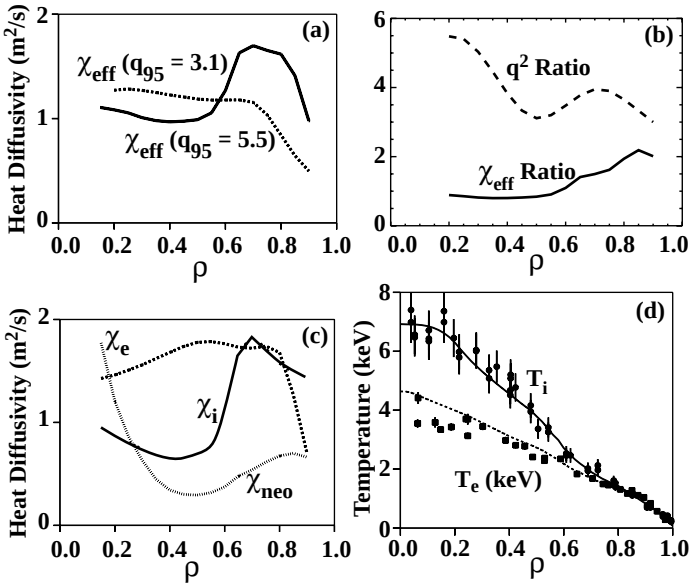

FIG. 7. Comparison of transport for a low q_{95} and a high q_{95} discharge with the same shape, size, and toroidal field (1.6 T). (a) One-fluid heat diffusivity vs. normalized radius; (b) ratios of χ_{eff} and q for the two discharges; (c) electron, ion, and neoclassical ion heat diffusivities for the high q_{95} discharge vs. normalized radius; (d) comparison of measured electron (squares) and ion (circles) temperature profiles vs. normalized radius with drift-wave model predictions for ion (solid line) and electron (dashed line) temperatures.

B. Impurity transport

Accumulation of impurities is a major concern for any high performance regime. In DIII–D, the dominant impurity is carbon due to 100% coverage of the vacuum vessel inside walls with graphite tiles. The carbon density profile is measured by spectroscopy of carbon atoms excited by charge exchange with the incoming neutral beam [23]. Previous work in discharges where the anomalous transport is low indicates the carbon density profile is consistent with that expected on the basis of neoclassical theory [24]. For high ion temperature plasmas, both the deuterium and carbon ions are expected to be in the collisionless regime. In this limit, neoclassical theory predicts the carbon transport will be dominated by the convective terms — one with velocity directed up the deuterium gradient and one directed down the ion temperature gradient. In cases where the deuterium gradient is small, the second term, called the temperature screening term, can lead to hollow impurity profiles.

The measured carbon and inferred deuterium profiles (Fig. 9) for the discharge shown in Fig. 3 at 1900 ms are qualitatively consistent with the neoclassical picture. At the middle radii, the deuterium gradient is nearly flat and the ion temperature gradient [Fig. 7(d)] is largest. This should lead to carbon piling up in the edge according to the neoclassical picture. This behavior is seen on the measured carbon profile. In the center, the deuterium profile peaks slightly while the ion temperature gradient weakens. This should lead to peaking of the carbon density, as is observed. Further evidence that the neoclassical effects are determining the shape of the profile is the long time scale (0.5–1 s) on which the central carbon accumulation occurs while total carbon content of the

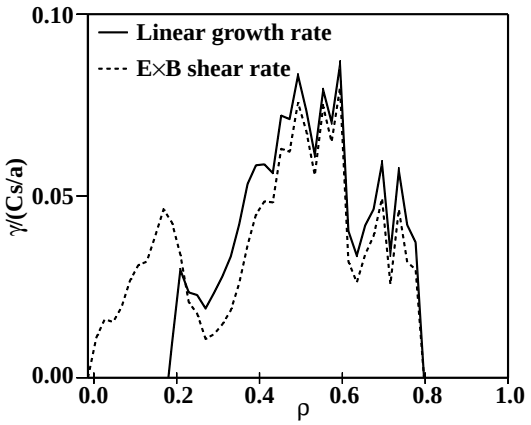

FIG. 8. Comparison of the normalized linear growth rate and normalized ExB shearing rate vs. normalized radius for the drift-wave model calculation.

plasma is constant. If neoclassical impurity transport governs the impurity density profile, then peaked deuterium density profiles will have deleterious consequences for impurity accumulation in the core in high performance discharges.

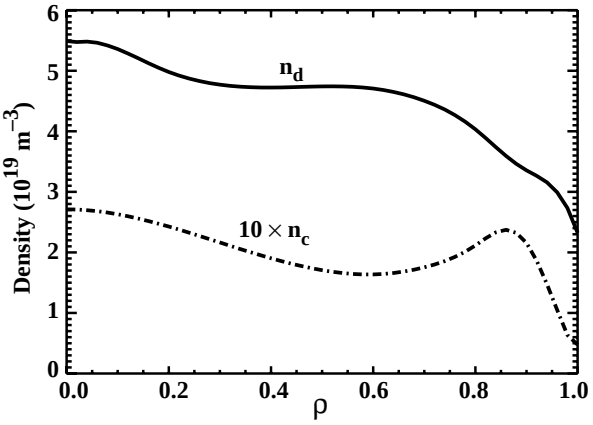

FIG. 9. Comparison of calculated deuterium density (solid line) and measured carbon density (dashed line) vs. normalized radius. The carbon density is multiplied by 10 to facilitate the comparison.

4. Current Profile Evolution

Control and sustainment of the current profile is a key element of an advanced tokamak. In Section 2, loss of both RWM and NTM stability were correlated with the evolution of the current profile. With the use of the motional Stark effect (MSE) diagnostic data [25] in the magnetic reconstruction [26], very accurate information about the total and inductive current profiles in DIII–D is available. From the measured total and inductive currents, the non-inductive current can be inferred and compared to models. Calculations of the required location and magnitude of the non-inductive current needed to reach steady state can also be made.

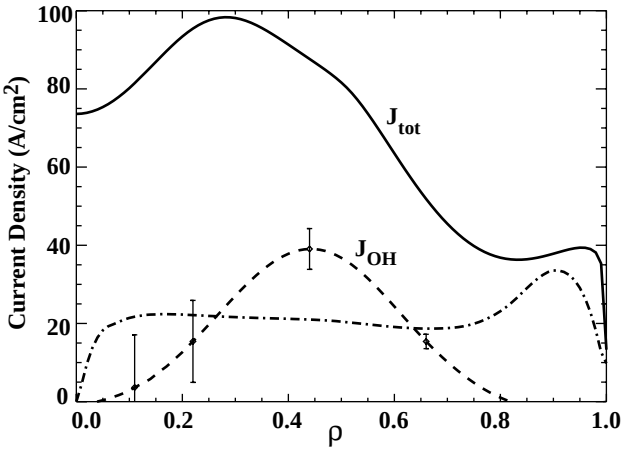

FIG. 10. Profiles of the total current density (solid line), Ohmic current density (dashed line), and calculated bootstrap current density (dot-dash line) profiles vs. normalized radius.

The technique employed to diagnose the current profile evolution requires a time history of the poloidal flux ψ. Spatial derivatives of ψ yield the current density J, while time derivatives of ψ give the parallel electric field $E_{||}$ [27]. Assuming neoclassical conductivity σ_{neo}, the measured profiles of T_e, and the impurity density, J_{ohm} can be obtained from $\sigma_{neo}E_{||}$. The difference between J and J_{ohm} is attributed to non-inductive current sources such as the bootstrap current and neutral beam current drive (NBCD). An analysis of the discharge shown in Fig. 3 at 1650 ms indicates the central and edge current are supplied non-inductively and the inductive current remaining is concentrated near the half radius (Fig. 10). The error bars indicate the uncertainty in J_{ohm} due to random uncertainties in $E_{||}$ from the analysis. The uncertainty near the axis is always larger with this technique because the conductivity is much larger there and small shifts in the magnetic axis in the reconstructions appear as $E_{||}$. An estimate of the bootstrap current using the Sauter model [28] is shown in Fig. 10. The total edge current is in rough agreement with the model, and the agreement is expected to improve if kinetic data were included in the equilibrium reconstruction. The central non-inductive current is attributed to the combination of bootstrap current and NBCD. Model calculations of the central current drive from these sources using the ONETWO [29] and TRANSP [30] codes show sufficient central current drive to sustain the measured total current density near the axis.

The analysis shown in Fig. 10 clearly points to the need for non-inductive current drive at the half radius. This conclusion is supported directly by the evolution of the total current density [Fig. 11(a)]. The peak of the current density just after the L–H transition is near the half radius and moves inward throughout the high performance phase. The proposed method to deliver the required non-inductive current in DIII–D is electron cyclotron current drive

(ECCD). However, as shown in Fig. 11(b), the density rises strongly at fixed β during the high performance phase. To maximize the amount of ECCD and to operate at relevant collisionality to minimize the extrapolation to a next-step tokamak, active control of the density is required. Demonstration of such control in ELMing H mode plasmas will be discussed in Section 5.

The correlation of heating power with current drive has a significant impact of the operational space in DIII–D. In order to lessen the external current drive requirements, it is desirable to maximize f_{BS}. One way to do this is to operate at higher q_{min} if the confinement is not reduced. The complete database with good equilibrium reconstructions using MSE data is displayed in Fig. 12. The achieved β_N is roughly independent of q_{min} for $1.0 < q_{min} < 1.8$. Above $q_{min} = 1.8$, with a single exception, the achieved β_N drops linearly with increasing q_{min}. Examination of these discharges does not show a β limiting instability. Instead, the evidence indicates strong overdrive of the central current by NBCD (Fig. 13) prevents access to high β at high q_{min}. The central loop voltage is negative [Fig. 13(a)] while the central current density is increasing. Since the only means at present of increasing β is through neutral beam injection which also drives central current, it does not seem possible to achieve higher q_{min} scenarios with neutral beam heating only.

The onset of Alfvén instabilities [bursting signals in Fig. 13(c)] also affects strongly the central NBCD. At 1150 ms, the loop voltage begins rising and becomes positive around 1300 ms. Calculations from similar discharges indicate that the NBCD and bootstrap should overdrive the total current density near the axis throughout the time shown.

In the future, some of the neutral beam power will be replaced with off-axis ECCD. This will lessen both the central NBCD and the drive for Alfvén modes. It is also possible to lower the NB accelerating voltage to reduce the central NBCD, since only half of the available

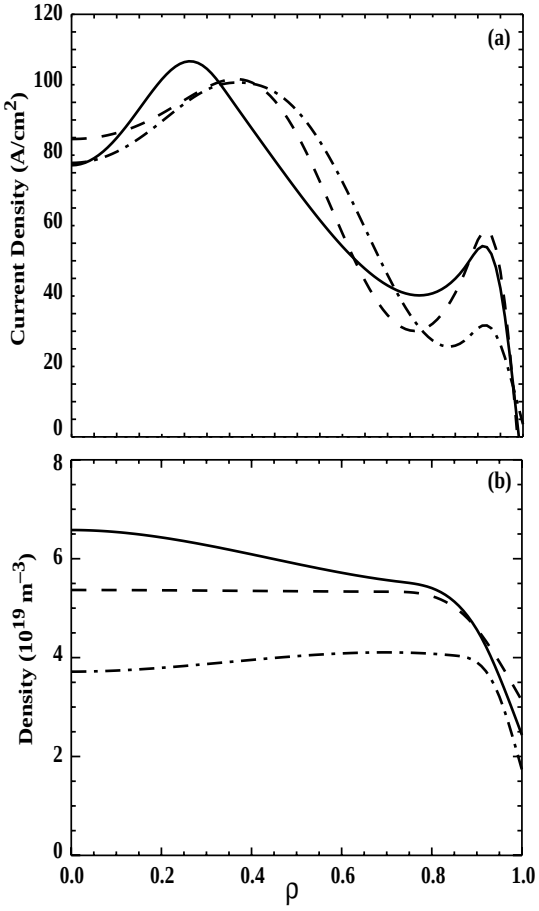

FIG. 11. Evolution of the (a) total current density and (b) electron density vs. normalized radius with time. In both boxes the dot-dashed curve is the profile at 1300 ms, the dashed curve is at 1600 ms, and the solid curve is at 1900 ms.

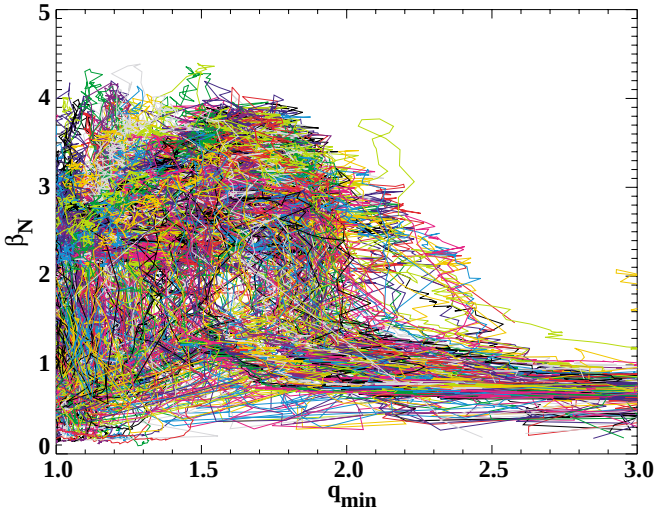

FIG. 12. Time histories of all 188 discharges with MSE data for the 1999 experimental campaign in β_N - q_{min} space. Each set of connected points are the results of magnetic reconstructions every 10 ms during a discharge.

power is required for this particular scenario. This should result in greater control over the details of the core current profile. It does not appear that fine control of the current profile is required at the present levels of β_N, since discharges which continue to evolve for up to 2 s at $\beta_N \sim 3.7$ do not encounter any instability which limits the duration. Operation closer to stability limits will require finer control of the pressure and current profiles at critical locations. The next section introduces demonstrations of some of the basic tools needed.

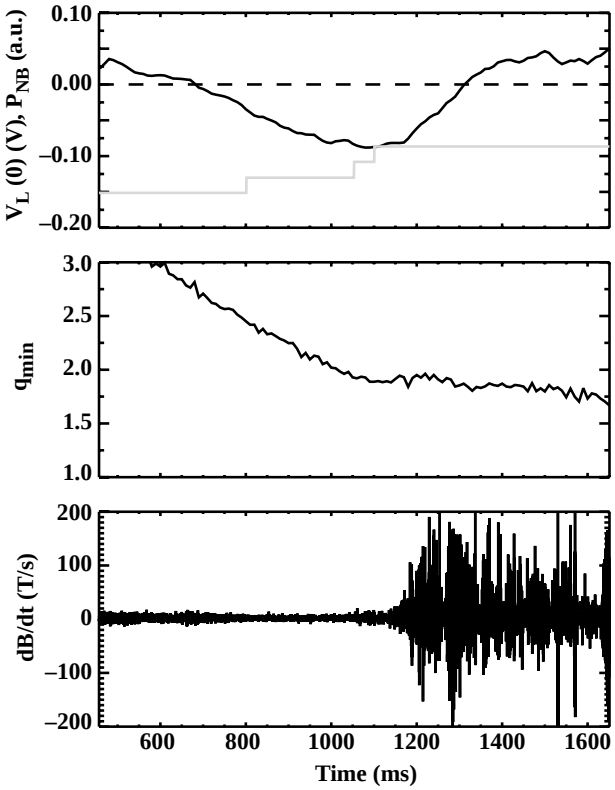

FIG. 13. Evidence for overdrive of the central current at high q_{min} and for Alfvén instabilities strongly reducing the central neutral beam current drive. (a) Loop voltage on axis (V) and neutral beam power (a.u.) vs. time; (b) q_{min} vs. time; (c) dB/dt from magnetic probes inside the vacuum vessel (T/s) vs. time.

5. Density and β Feedback Control

It is likely that advanced tokamak scenarios will require active control to remain at the desired point in operational space. The ultimate realization of this will require detailed control of the profiles. At present, the control of these profiles on DIII-D is available only on a transient basis. However, tools have been developed to finely control critical global parameters (e.g., density and β) at levels necessary for optimization of advanced tokamak scenarios.

Control of the density in high performance plasmas is necessary to achieve the advanced tokamak goals set out for DIII–D. For this purpose, divertor pumps and baffling suitable for particle control in high triangularity plasmas have been installed in the upper divertor in DIII–D (Fig. 14). The newest addition during the last vacuum opening (Oct.–Dec. 1999) was a cryopump in the private flux region with an aperture suitable to pump the inner divertor leg [31]. The pump is protected by a graphite-covered dome which also has the effect of reducing the volume available for neutrals and plasma in the private flux region.

Since the density scrape-off layer is ≈1 cm at the midplane of DIII–D, it is necessary to place the separatrix such that the pump aperture is at or inside the field line which maps back to 1 cm outside the last closed flux surface at the midplane. This level of precision required development of algorithms for independent control of the locations where the separatrix strikes the divertor on both outer and inner divertor leg. These control algorithms were implemented on the real-time digital plasma control system (PCS), which updates the shape control every 1.5 ms [32]. Dedicated experiments have demonstrated independent simultaneous control of inner and outer strike points in the upper divertor, the lower X point, and the balance between the upper and lower X point. The strike point positions in the upper divertor have been verified using Langmuir probes embedded in the divertor tiles to an accuracy of about 5 mm.

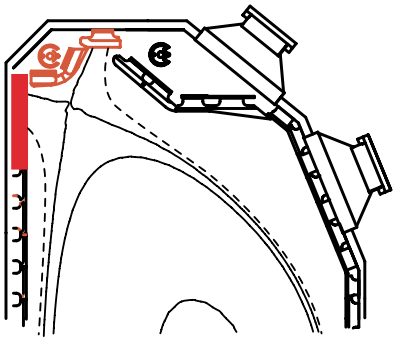

FIG. 14. Upper divertor hardware presently installed in DIII–D. The dashed line is the flux contour which is 1 cm in radius outside the last closed flux surface at the midplane.

The main challenge for controlling density in the H mode phase is to limit the density rise following the L–H transition. It is necessary to control the particle inventory of the wall, because the pumping speed of the plasma is much greater than that of the two cryopumps. Pumping during the L–mode current ramp phase is found to be very effective at depleting the wall inventory and limiting the H–mode density rise (Fig. 15). The degree of pumping in the current ramp was varied by shifting the balance of the divertor nulls from lower dominant (no pumping) to upper dominant (strong pumping). The balance of the divertor nulls is quantified by evaluating the radial distance at the midplane of the field lines attached to the two nulls (dRsep). By convention, positive values of dRsep mean the upper null is dominant (right side of Fig. 15), while negative is lower null dominant (left side of Fig. 15). A perfectly balanced double null is denoted by dRsep = 0. For all the discharges shown in Fig. 15, the density follows the same time history through feedback-controlled gas puffing. Despite a larger gas input, the wall inventory inferred from particle balance is lower and the density rise rate is smaller in the strong pumping cases. Because the high triangularity pumps are only in the upper divertor, it is necessary to have dRsep > 0 to ensure there is no significant fueling in the lower divertor from recycling on the floor. A dRsep of 5 mm was found to be sufficient for good density control. Control was demonstrated by simultaneously gas puffing and pumping at fixed shape. No degradation of confinement was observed during gas puffing.

Attempts to operate at high β_N in a shape suitable for pumping (left side of Fig. 16) at the same normalized current ($I_N \equiv I/aB$) as the β_N H_{89} ~ 10 discharges encountered a lower RWM β limit. The parameter *S* is defined as I_N q_{95} and is a measure of how shaped the plasma is [33].The discharge of Fig. 3 (shown at the right in Fig. 16) has an *S* = 6.7 while a symmetric double null with the strike points positioned for optimum pumping has only *S* = 5.2. Rounding the bottom with dRsep > 0 to eliminate the recycling in the lower divertor further reduces *S*. Theoretical studies of ideal n=1 stability with fixed pressure gradient and fixed q profile indicate a significant variation of the β limit with *S* in this range [34]. Whether the RWM stability should have the same theoretical dependence on *S* is not yet known. By a series of experiments eliminating potential differences in q profile and other parameters, it appears that some aspect of the shape is the key difference in the β limits of the two discharges whose cross sections are shown. The shape studies shown in Fig. 16 were carried out at fixed I and B. It is possible that the q_{95} and profile variation with shape rather than the intrinsic properties of the shapes themselves lead to the variation of the β limits.

Operation near a stability limit will require precise control of β. On DIII–D, this is accomplished by feedback control of the neutral beam power by the PCS, based on measurements of the diamagnetic flux. A key new feature is the ability to enable the

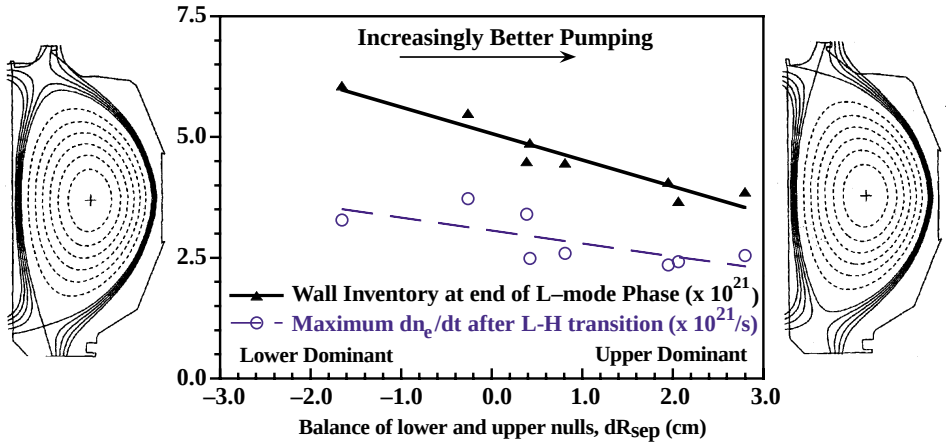

FIG. 15. Effect of pumping during the current ramp on wall inventory (triangles) and the maximum rate of density rise (circles) after the L-H transition. The magnitude of the pumping is correlated with the relative location in flux space of the two divertor nulls (horizontal axis). The vertical axis is number of particles for the wall inventory and particles/s for the rate of density rise. The flux contours on either side give an example of dRsep < 0 (left) and dRsep > 0 (right). The quantity dRsep is defined in the text.

feedback at a preset level rather than a fixed time. This allows control of the β beginning shortly after the L–H transition, independent of jitter in the timing of the transition. Early control helps protect against overshoot during the ELM-free period which can destabilize MHD modes. This control can also simulate the stop in the β rise caused by the Alfvén modes.

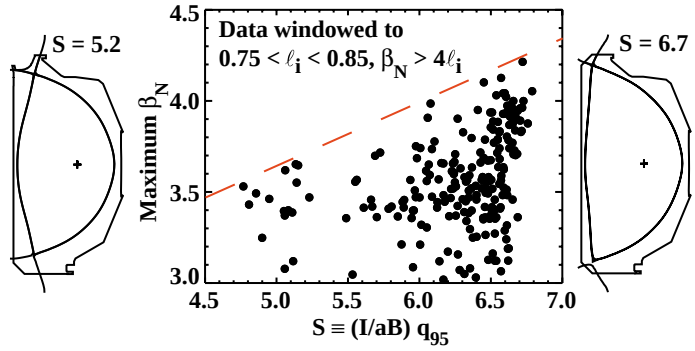

FIG. 16. The β_N limit vs. shape parameter S. The data is windowed for data with $\beta_N > 4\ \ell_i$ to select discharges which should be limited by resistive wall modes, and windowed for $0.75 < \ell_i < 0.85$ to remove some of the expected variation with ℓ_i. Narrower windows in ℓ_i throughout 0.75-0.85 show the same dependence with a smaller number of discharges.

A very nice demonstration of the control capabilities of the PCS and the suitability of the DIII–D tokamak for long-pulse high-performance studies is shown in Fig. 17. Using density and β regulation, a discharge with $\beta_N H_{89} \sim 7$ was run for 6.3 s or about 34 τ_E or >3 τ_R. The neutral beams were feedback-controlled as shown in Fig. 17(a) to yield β_N = 2.7. The density was maintained by gas puffing and pumping at n = 3.6 x 10^{19} m^{-3}. At about 1350 ms, a small m=3/n=2 mode appears and remains throughout the discharge with apparently little impact of confinement since the H_{89} remains above 2.5. After less than 2 s at high β_N, the discharge appears to reach resistive equilibrium based on the MSE pitch angle time histories (Fig. 18). The discharge does not have sawtooth oscillations or fishbones, and equilibrium reconstructions indicate a stationary q profile with q(0) just above 1. The discharge terminates at 7.6 s only because of a control interlock for one of the poloidal field coils. No fundamental time duration limitations of the DIII–D power supplies or vessel were encountered. About 48 MJ of energy was injected during this pulse. Infrared camera measurements of the upper divertor tiles showed center tile temperatures nearing 1100°C. Tile edges are likely hotter, possibly approaching the sublimation point, but no increased carbon source was observed.

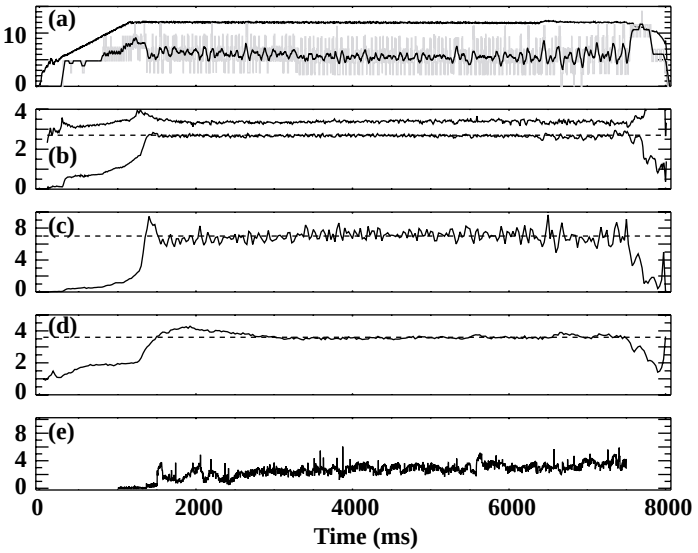

FIG. 17. Long-pulse demonstration of density and β control. (a) Plasma current x 10 (MA) (upper trace), actual neutral beam power (MW) (light trace), and averaged (50 ms) neutral beam power (MW) (lower trace) vs. time; (b) 4 x ℓ_i (upper trace) and β_N (lower trace) vs. time; (c) $\beta_N H_{89}$ vs. time; (d) line-averaged density (10^{19} m^{-3}) vs. time; (e) amplitude of n=2 magnetic oscillations (G) vs. time. The dashed lines in (b) and (d) show the requested value of β_N and ⟨n⟩, respectively. The dashed line in (c) is $\beta_N H_{89}$ = 7.

The quality of β control is demonstrated by the fact that discharges were sustained for >5 s at 95% of the m=2/n=1 tearing mode β limit. The two discharges shown in Fig. 19 differ in the requested β value by 5%. The higher β discharge triggers an m=2/n=1 tearing mode on an upward fluctuation in β. This tearing mode leads to a dramatic loss of confinement (β_N drops 12% despite a 60% increase in power). After 1.2 s, the plasma disrupts, but only due to the vertical position feedback being disabled, not the tearing mode locking. A more sophisticated

control algorithm would have plenty of time to detect the degraded confinement and shut the plasma down. More than 20 discharges were reproducibly operated just below the stability limit for >3 s, limited only by control hardware or operator programmed duration.

6. Discussion and Future Prospects

The discharges discussed which have $\beta_N H_{89} \sim 10$ are an excellent starting point for a fully non-inductive advanced tokamak demonstration. The β is limited in these discharges by the resistive wall mode. The main issue for both maintaining stability and fully non-inductive operation is development of an off-axis non-inductive current drive capability. The possibility of fully non-inductive discharges in DIII–D depends critically on the ECCD efficiency obtained, which in turn depends on the level of density control and electron confinement. If more bootstrap current is needed, one possibility is operation at higher q_{min}. This requires substitution of heating power which does not drive central current. All of these issues point out the key role of ECCD in the DIII–D Advanced Tokamak Program.

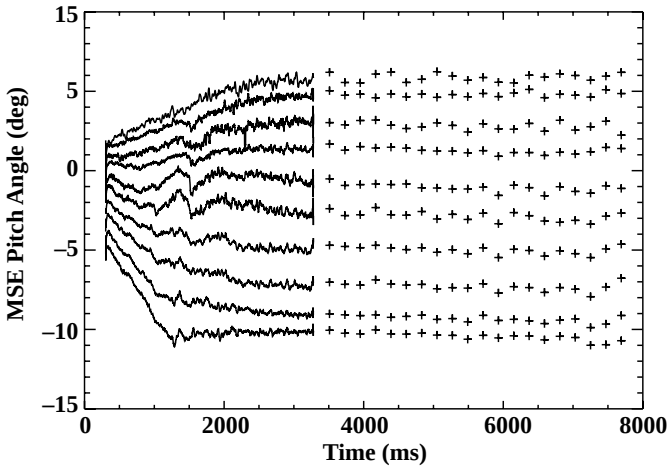

FIG. 18. MSE pitch angle measurements from $\rho = 0.25$ on the high field side (upper trace) to $\rho = 0.45$ on the low field side (lower trace) vs. time. Other MSE arrays measure the pitch angle on the low field side out to the plasma edge.

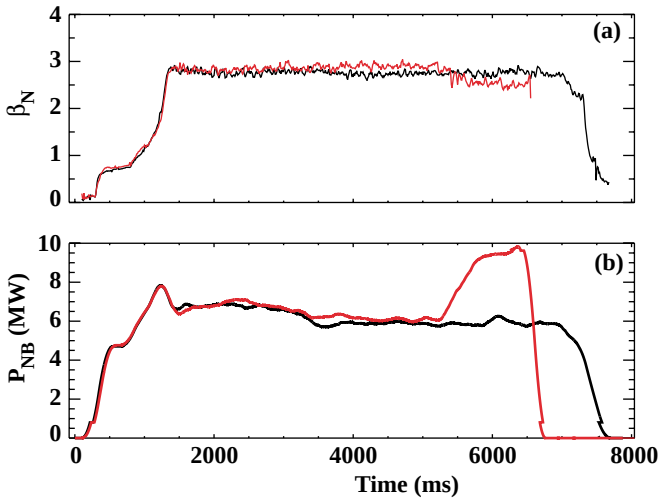

FIG. 19. Demonstration of operation at 95% of the m=2/n=1 tearing mode stability limit. (a) β_N vs. time; (b) averaged (200 ms) neutral beam power (MW) vs. time. The higher β_N discharge has a m=2/n=1 tearing mode triggered by a fluctuation in β at 5200 ms. Operation at 5% smaller request for β in the feedback results in reproducible stable operation. The tearing mode occurs at a time when the current profile appears to be in resistive equilibrium (cf. Fig. 18).

Successful implementation of the active RWM stabilization system currently under development at DIII–D [15] will lead to higher β operation. Design studies indicate that an optimized system can provide stabilization of the RWM nearly up to the ideal-wall ideal n=1 limit. Raising β would increase f_{BS}, in turn lessening the requirements on the external non-inductive current source. Stability of NTMs may become an issue at higher β. The first experiments in DIII-D to stabilize NTMs with ECCD have been successfully carried out [35]. Several of the basic control issues for an advanced tokamak have been successfully addressed on DIII–D. These were demonstrated by the long-pulse high-performance ELMing H modes with $\beta_N H_{89} \sim 7$. Real-time q profile calculations, which are a necessary step for true current profile control, will be available in the coming year. Combined with the possibility of multiple steerable launchers for the EC system and the ability to feedback control the neutral beams, a significant demonstration of β and current profile control should be possible in the near future.

Acknowledgments

This is work was supported by the U.S. Department of Energy under Contract Nos. DE-AC03-99ER54463, DE-AC05-00OR22725, W-7405-ENG-48, DE-AC02-76CH03073, DE-AC04-94AL85000, and Grant Nos. DE-FG03-97ER54415, and DE-FG02-89ER53297.

References

[1] ITER Physics Basis, Nucl. Fusion **39**, 2137 (1999).
[2] BICKERTON, R.J., et al., Nature (Phys. Sci.) **229**, 110 (1971).
[3] KESSEL, C., MANICKAM, J., REWOLDT, G.W., TANG, W.M., Phys. Rev. Lett. **72**, 1212 (1994).
[4] TURNBULL, A.D., et al., Phys. Rev. Lett. **74**, 718 (1995).
[5] LAO, L.L., et al., Phys. Plasmas **3**, 1951 (1996).
[6] ITER Physics Basis, Nucl. Fusion **39**, 2175 (1999).
[7] YUSHMANOV, P.N., et al., Nucl. Fusion **30**, 1999 (1990).
[8] STRAIT, E.J., et al., Phys. Plasmas **4**, 1783 (1997).
[9] RICE, B.W., et al., Nucl. Fusion **39**, 1855 (1999).
[10] RICE, B.W., et al., Plasma Phys. Control. Fusion **38**, 869 (1996).
[11] STRAIT, E.J., Phys. Plasmas **1**, 1415 (1994).
[12] FERRON, J.R., et al., Phys. Plasmas **7**, 1976 (2000).
[13] BONDESON, A., WARD, D.J., Phys. Rev. Lett. **72**, 2709 (1994).
[14] BERNARD, L.C., HELTON, F.J., MOORE, R.W., Comput. Phys. Commun. **24**, 377 (1981).
[15] GAROFALO, A.M., et al., Nucl. Fusion **40**, 1491 (2000).
[16] GIMBLETT, C.G., HASTIE, R.J., Phys. Plasmas **7**, 258 (2000).
[17] LA HAYE, R.J., RICE, B.W., STRAIT, E.J., Nucl. Fusion **40**, 53 (2000).
[18] HAZELTINE, R.D., HINTON, F.L., Rev. Mod. Phys. **48**, 239 (1976).
[19] PETTY, C.C., et al., Phys. Plasmas **5**, 1695 (1998).
[20] PETTY, C.C., LUCE, T.C., Phys. Plasmas **6**, 909 (1999).
[21] WALTZ, R.E., et al., Phys. Plasmas **5**, 1784 (1998).
[22] KOTSCHENREUTHER, M., Bull. Am. Phys. Soc. **37**, 1432 (1992).
[23] GOHIL, P., et al., in Proc. of the 14th Symposium on Fusion Engineering, San Diego, California, 1992 (IEEE, New York, 1992), Vol. 2, p. 1199.
[24] WADE, M.R., HOULBERG, W.A., BAYLOR, L.R., Phys. Rev. Lett. **84**, 782 (2000).
[25] RICE, B.W., et al., Phys. Rev. Lett. **79**, 2694 (1997).
[26] LAO, L.L., et al., Nucl. Fusion **30**, 1035 (1990).
[27] FOREST, C.B., et al., Phys. Rev. Lett. **73**, 2444 (1994).
[28] SAUTER, O., ANGIONI, C., LIN-LIU, Y.R., Phys. Plasmas **6**, 7834 (1999).
[29] ST JOHN, H.E., TAYLOR, T.S., LIN-LIU, Y.R., TURNBULL, A.D., Plasma Physics and Control. Nucl. Fusion Research, Seville, 1994 (IAEA, Vienna, 1995) Vol. 3, p. 603.
[30] HAWRYLUK, R.J., et al., Physics Close to Thermonuclear Conditions (Proc. Course, Varenna, 1979) Commission of the European Communities, Brussels (1979).
[31] MAHDAVI, M.A., et al., "Initial Performance Results of the DIII-D Divertor 2000," accepted for publication in J. Nucl. Mater.
[32] FERRON, J.R., et al., Nucl. Fusion **38**, 1055 (1998).
[33] LAZARUS, E.A., et al., Phys. Fluids B **4**, 3644 (1992).
[34] TURNBULL, A.D., et al., Nucl. Fusion **38**,1467 (1998).
[35] PRATER, R., et al., this conference.